

The Keck Aperture Masking Experiment: Near-Infrared Sizes of Dusty Wolf-Rayet Stars

J. D. Monnier¹, P. G. Tuthill², W. C. Danchi³, N. Murphy^{1,4} and T. J. Harries⁵

ABSTRACT

We report the results of a high angular resolution near-infrared survey of dusty Wolf-Rayet stars using the Keck-1 Telescope, including new multi-wavelength images of the pinwheel nebulae WR 98a, WR 104, and WR 112. Angular sizes were measured for an additional 8 dusty WR stars using aperture masking interferometry, allowing us to probe characteristics sizes down to ~ 20 milliarcseconds (~ 40 AU for typical sources). With angular sizes and specific fluxes, we can directly measure the wavelength-dependent surface brightness and size relations for our sample. We discovered tight correlations of these properties within our sample which could not be explained by simple spherically-symmetric dust shells or even the more realistic “pinwheel nebula” (3-D) radiative transfer model, when using optical constants of Zubko. While the tightly-correlated surface brightness relations we uncovered offer compelling *indirect* evidence of a shared and distinctive dust shell geometry amongst our sample, long-baseline interferometers should target the marginally-resolved objects in our sample in order to conclusively establish the presence or absence of the putative underlying colliding wind binaries thought to produce the dust shells around WC Wolf-Rayets.

Subject headings: stars: binaries — stars: Wolf-Rayet — stars: wind — radiative transfer — instrumentation: interferometers — circumstellar matter — stars: individual (WR 11, Gamma Vel, WR 48a, WR 76, WR 95, WR98a, WR 104, WR 106, WR 112, WR 113, WR 118, WR 140, CV Ser)

¹University of Michigan, Department of Astronomy, Ann Arbor, MI 48109

²University of Sydney, Australia

³NASA-Goddard Space Flight Center

⁴Now at the University of Wisconsin, Department of Astronomy

⁵University of Exeter, England

1. Introduction

The existence of dust shells around Wolf-Rayet stars has long posed a mystery: how can dust nucleate and survive near these hot stars in the presence of harsh ultraviolet radiation and gas densities lower than those found in other dust forming environments (e.g., AGB winds)? While novel chemical pathways for producing special carbonaceous grains have been proposed (Zubko 1998; Cherchneff et al. 2000), recent theoretical and observational results point strongly to a very different solution.

Inspired by the periodic dust formation episodes around the colliding wind binary WR 140 (Moffat et al. 1987; Williams et al. 1990b), Usov (1991) suggested that dust formation might be catalyzed in the compressed layer of gas at the interface of colliding winds in WR+OB binary systems. This hypothesis was confirmed by the surprising imaging of a “pinwheel” nebula dust spiral around WR 104 (Tuthill et al. 1999b). Indeed, Monnier et al. (1999a) went so far as to suggest that perhaps *all* dusty WR systems are hiding colliding-wind binary systems (see also Dougherty & Williams 2000a) and this was further supported by the discovery of non-thermal radio emission around WR 104, WR 98a, and WR 112 (Monnier et al. 2002b).

The previously-cited imaging work was carried out using the diffraction-limited capabilities of the world’s largest optical telescope at the Keck Observatory. High-resolution imaging was achieved using aperture masking interferometry, whereby the Keck-1 primary mirror is converted to a VLA-style interferometric array (Tuthill et al. 2000c) of many subapertures. This technique has been shown to be superior than current adaptive optics systems for high-fidelity imaging and size estimations for marginally-resolved objects (Rajagopal et al. 2004).

Here we report an extension to the initial imaging work of WR 104 and WR 98a. We observed all WR stars (accessible from Mauna Kea) brighter than m_K 6.5 in order to investigate the binary hypothesis as to the origin of dust production. Although imaging was only possible for one additional source (WR 112), we report the characteristic size measurements for a total of 11 sources and discuss the significance of these findings.

2. Observations

Our group has been carrying out aperture masking interferometry at the Keck-1 telescope since 1996. We have published images and size measurements with unprecedented angular resolution on topics ranging from young stellar objects, carbon stars, red supergiants, and photospheric diameters of Mira variables (e.g., Monnier et al. 1999c; Tuthill

et al. 2000a,b; Danchi et al. 2001). A full description of this experiment can be found in Tuthill et al. (2000c), with further discussion of systematic errors in Monnier et al. (2004).

The NIRC camera with image magnifier (Matthews et al. 1996) was used in conjunction with the aperture masking hardware. For this work, we used an aperture mask with an annulus that is 8-m in diameter as projected onto the Keck primary. This mask gives us complete UV coverage and sensitivity for targets brighter than $m_K \sim 6$ with a modest loss in calibration precision due to additional redundancy noise (for further discussion, see Tuthill et al. 2000c). The data frames were taken in speckle mode ($T_{\text{int}}=0.14$ s) to freeze the atmosphere. A variety of filters were used and the characteristic center wavelengths and widths can be found in Table 1 (spectral scans can be found in Keck-NIRC users manual).

Here we report the full body of Wolf-Rayet size measurements collected during the entire period of the Keck aperture masking experiment. A target list and observing log can be found in Tables 2 & 3. All V^2 and closure phase data are available from the authors; all data products are stored in the FITS-based, optical interferometry data exchange format (OI-FITS), recently described in Pauls et al. (2005).

3. Determining Characteristic Sizes

3.1. Methodology

While the basic data reduction has been described in previous papers (Tuthill et al. 2000c), this paper is the first Keck aperture masking paper to explicitly deal with a sample of partially-resolved objects. This is important here since we intend to measure the 2-dimensional size and shape of Wolf-Rayet dust shells in order to search for asymmetries. If we measure an ellipticity in our data, what confidence do we have that an elongation is not due to poor calibration of the optical transfer function? To answer this question we have undertaken a systematic investigation of our calibration errors.

The errors for this experiment are dominated by statistical and seeing calibration errors. The statistical error arises from the contribution of photon noise and read noise to our measurement process. Calibration error arises because the optical transfer function varies with time and telescope pointing. In order to correct for this latter effect, we always observe a point-source reference star nearby in time and angle from our target. In the process of calibration, raw visibilities from the target are divided by those from the calibrator. Hence, calibration error is multiplicative and affects high visibility data the most in absolute terms (ΔV). For well-resolved objects, these two types of error are comparable. For small objects ($\lesssim 25$ mas) calibration error is dominant and limits our ability to say whether an object is

resolved.

3.1.1. Functional Form and Statistical Errors

As part of our analysis, the calibrated visibility data are fit to the following generic function (based on a 2-dimensional Gaussian):

$$V^2 = [V_o e^{-(\alpha u^2 + \beta v^2 + \gamma uv)} + V_P]^2, \quad (1)$$

where V_P is constant and represents a point source contribution (which was set to zero for this study). The parameters α , β , and γ are not constrained to be positive, thus allowing the function to curve upwards in cases where calibration errors are extreme.

Under a rotation through angle ϕ , this function can be projected onto the major and minor axes (u', v') , written in the form

$$V^2 = \left[V_o e^{-4 \ln 2 \left[\left(\frac{u'}{u'_{\text{FWHM}}} \right)^2 + \left(\frac{v'}{v'_{\text{FWHM}}} \right)^2 \right]} + V_P \right]^2 \quad (2)$$

with the parameters of this fit being given by

$$\phi = \frac{1}{2} \arctan \left(\frac{\gamma}{\alpha - \beta} \right) \quad (3)$$

$$(u'_{\text{FWHM}})^2 = \frac{4 \ln 2 \cos 2\phi}{\alpha - (\alpha + \beta) \sin^2 \phi} \quad (4)$$

$$(v'_{\text{FWHM}})^2 = \left[\frac{\alpha + \beta}{4 \ln 2} - \frac{1}{(u'_{\text{FWHM}})^2} \right]^{-1} \quad (5)$$

These expressions can be converted to the angular FWHM along the major/minor axis using the formula $\text{FWHM}_{\text{Major}} = \frac{4 \ln 2}{\pi u'_{\text{FWHM}}}$ and $\text{FWHM}_{\text{Minor}} = \frac{4 \ln 2}{\pi v'_{\text{FWHM}}}$

Statistical errors are dealt with by using bootstrap sampling (Efron & Tibshirani 1993) with the function given in Equation 1. The fitting routine **MPFIT** in Craig Markwardt's **MINPACK**¹ suite of IDL programs is used as the basis for the bootstrap.

¹See <http://cow.physics.wisc.edu/~craigm/idl/>

3.1.2. Monte-Carlo Method for Determining Calibration Error

Quantifying the magnitude of calibration errors in this experiment has been difficult. Due to the very limited time available on a Keck telescope, the number of stars used as calibrators for a given filter is usually small, ranging from less than 5 up to perhaps a dozen for the most commonly used bands. While precise systematic errors are difficult to determine due to small number statistics, it is possible to estimate the magnitude of the calibration accuracy.

The first step in the analysis of calibration errors is to cross-calibrate all of the calibration stars of a given night (with same bandpass filter and aperture mask) against each other and fit the resulting visibility curves with the quadratic function introduced in the last section (Eq.2). At this point, the calibrator-calibrator pairs are weighted according to proximity to each other in time and elevation according to $e^{-\left(\frac{\Delta t}{\Delta t_*}\right)^2 - \left(\frac{\Delta \theta_{el}}{\Delta \theta_{el*}}\right)^2}$ with $\Delta t_* \sim 2000$ s and $\Delta \theta_{el*} \sim 20^\circ$.

In order to propagate calibration errors into the errors on the Gaussian FWHM sizes that we wish to measure, we start with a visibility curve with a known FWHM (using the same baselines as the Keck data). Then we multiply this perfect simulated data by various calibrator-calibrator pair data and then re-calculate a size using the quadratic model developed above. This simulates what the measured visibility would look like for a star of a known size using different calibrators. By Monte Carlo sampling over many cal-cal pairs according the weights described above, we build up an estimate of the likely error in the final size measurement.

The results are summarized in Figure 1 for the 2000 June epoch in the CH4 filter using the Annulus mask. The most important feature of these plots is determination of the effective angular resolution limit of this experiment. We see that simulations of an unresolved point source, when passed through the calibration study described above, can yield apparent sizes as large as 12 milliarcseconds (Gaussian FWHM). From this, we conclude that our resolution limit corresponds to Gaussian FWHMs of 12-15 mas ($\lambda \sim 2.2\mu\text{m}$), approximately $4\times$ better than the formal Keck diffraction limit $1.22\lambda/D \sim 55$ mas. For nights of poor seeing, our size upper limit on FWHM increases to 15-20 mas.

As stated before, we would like to use the Keck masking data to measure modest asymmetries in the dust shells of Wolf-Rayet stars, since this can tell us about the dust production mechanism (single-star vs binary interaction). In order to test our sensitivity to asymmetries, we fitted 2-D Gaussians to our calibrator study data and these results are also shown in Figure 1. Our study shows that if we impose typical calibration errors on a circularly symmetric object with FWHM 20 mas, we will regularly find asymmetries with

measured ratio $\text{FWHM}_{\text{minor}} / \text{FWHM}_{\text{major}} = 0.8$. Thus, except for extremely asymmetric objects, any study on asymmetries from this data will have to restrict itself to objects that are larger than about $\gtrsim 25\text{-}30$ mas.

We note that the calibration errors determined by this method are over-estimates, since typical calibrator-calibrator pairs suffer from greater time difference and angular distance than target-calibrator pairs used for actual science measurements (this is confirmed for a few objects where we have multiple independent data sets). Thus we can assume that the errors calculated in this section are conservative and the true calibration errors should be up to a factor of 1.5 to 2 smaller for nights of comparable seeing.

The greatest uncertainty in this analysis is that it uses a very limited number of calibrator stars spread out over a night. Our understanding of the errors would improve greatly if a series of identical exposures of a calibrator star were to be taken sequentially². This would allow us to see the short timescale variations in a calibrator’s visibility curve, and thus how much variance there is in the calibration process. If very large variations in the quadratic fits remain on timescales as short as this, the calibration process may need further refinement.

The same study has been done for H band ($\lambda = 1.65\mu\text{m}$) and PAHcs ($\lambda = 3.08\mu\text{m}$), and these results are also included (in the same format) in Figures 2 & 3.

4. Results

4.1. Multi-wavelength Characteristic Sizes

Circularly-symmetric gaussian emission profiles were fitted to the azimuthally-averaged visibility data for all targets and the results can be found in Table 4. The uncertainty estimates were based on the combined error from statistical variations (using bootstrap) and from the calibration errors discussed in the last section. Calibration error is typically the dominant error for these data.

The largest dust shells (WR 48a, WR 98a, WR 104, WR 112, and WR 140) show strong deviations from the Gaussian at the longer Keck baselines. This is not at all surprising since WR 98a, WR 104, WR 112 and WR 140 are all known to have spiral and/or asymmetric dust shells (Tuthill et al. 1999b; Monnier et al. 1999a; Ragland & Richichi 1999; Monnier et al. 2002d; Marchenko et al. 2002). It is likely that the other smaller dust shells in our sample are also not simple Gaussians, although we were unable to detect deviations due

²The Keck Time Allocation Committee is unlikely to give time to such a proposal

to insufficient angular resolution (all marginally resolved objects look Gaussian-like to an interferometer).

In order to calculate a consistent “characteristic size” for all targets, we only fit to short-baseline data where the visibility is greater than 0.5. By fitting only to short-baseline, high-visibility data, the reported characteristic sizes represent the overall scale of emission and are not strongly affected by the spiral and/or small-scale structures of the nebulae, if present. Our results are graphically shown for $2.2\mu\text{m}$, $1.65\mu\text{m}$ and $3.08\mu\text{m}$ in Figures 4-6.

Subject to the (large) uncertainties in ellipticity discussed in §3.1.2, we did not find evidence for elongation in the emission except for the cases of the largest dust shells, WR 98a, WR 104, and WR 112. For these, we have reported the mean Gaussian FWHM and the ratio of the minor axis to the major axis. Just as for the characteristic sizes discussed above, this ellipticity parameter only refers to the “large-scale” emission component of the dust shell and not the smaller-scale details, such as the inner spiral windings of WR 104.

4.2. Correction for Stellar Contribution

While for most stars the near-infrared emission is completely dominated by dust emission, some targets in our sample have significant stellar contributions. By carrying out simple spectral energy density (SED) fitting, we can estimate the fraction of light coming from the star (compared to dust) and apply a correction factor. Essentially the visible photometry is fit with a Kurucz model allowing the stellar size and reddening to vary; the stellar IR flux can then be estimated by extrapolation. With this knowledge, we can more accurately estimate the true size of the dust shell (not the star+dust emission). This is a common procedure in other areas of astronomy, such as estimating the sizes of disks around young stellar objects, and we follow procedures documented elsewhere (e.g., Millan-Gabet et al. 2001; Monnier et al. 2005).

This correction is strongest for γ Vel (WR 11) which does not show much infrared excess, but since the observed characteristic size was consistent with a point source, we do not apply the correction. For cases where the correction is more than 5% (WR 48a, WR 95, WR 98a, WR 106, WR 113), we have included the new size estimates (and the estimates for the dust fraction) in Table 5. We estimate the correction factor is only known to 50% due to difficulty in uniquely fitting the broadband SEDs, and this error has been included in the corrected sizes in Table 5.

Note that the post-outburst WR 140 dust shell is so large that it was obviously necessary to correct for the stellar contribution (see top curves of Figure 4) and this was done for

Table 4. The WR 140 dust shell was considered in detail in Monnier et al. (2002d) and we refer the reader to this paper for further discussion on this object.

4.3. Aperture Synthesis Imaging

Three systems in our sample are sufficiently resolved that they can be imaged using aperture synthesis techniques. The Maximum Entropy Method (MEM) (Skilling & Bryan 1984; Gull & Skilling 1983) has been used to create diffraction-limited images from the interferometric data, as implemented in the VLBMEM package by Sivia (1987).

Figures 7-9 show new multi-wavelength images of WR 98a, WR 104, and WR 112 at wavelengths of $1.65\mu\text{m}$, $2.2\mu\text{m}$, and $3.08\mu\text{m}$. The resolution degrades with increasing wavelength and we adopt an effective angular resolution of 21 mas, 28 mas, and 39 mas for $1.65\mu\text{m}$, $2.2\mu\text{m}$, and $3.08\mu\text{m}$, corresponding to $\Delta\Theta = \frac{\lambda}{2B_{\text{mas}}}$. While we have presented images of WR 98a and WR 104 in the past, images given here are at a new epoch and we have included additional wavelengths.

Figure 9 contains the first published resolved images of the near-infrared dust shell around WR 112 (preliminary results were shown at the “Interacting Winds from Massive Stars” workshop in 2000; Monnier et al. 2002a). The asymmetric nature of this dust shell was already discovered using lunar occultations (Ragland & Richichi 1999). Recently, Marchenko et al. (2002) reported a spiral-like dust plume around WR 112 at *mid-infrared* wavelengths. Interestingly, we do not see an obvious spiral structure in these new near-infrared images, rather we see only evidence for filaments/arcs and one-sided nebulosity.

5. Discussion

This paper significantly expands the number of WR stars with known angular sizes. and we wish to use this information to probe the nature of the dusty outflows so common in WC systems. The Wolf-Rayet systems with the largest dust shells, WR 48a, WR 98a, WR 104, WR 112, WR 140, are *all in confirmed colliding wind systems* (from detection of non-thermal radio emission). Unfortunately, we do not have enough angular resolution to definitely resolve filamentary or spiral structure in the other objects in our survey.

5.1. Surface Brightness Relations

Secure identification of binarity is critical – Monnier et al. (1999a) emphasize that if all dusty WR stars are in binaries that this has profound implications on massive stellar evolution and the nature of carbon-rich (WC) WR stars in particular. One method to achieve this end is to see if all the objects in our survey follow similar *surface brightness relations*. In order to calculate a specific surface brightness S_λ we applied the following formula:

$$S_\lambda = \frac{F_\lambda 10^{-(\text{mag}/2.5)}}{0.68\pi\Theta_{\text{FWHM}}^2} \quad (6)$$

where F_λ represent the flux density for a zero magnitude star (here using units of $\text{W m}^{-2}\mu\text{m}^{-1}$), mag is the magnitude of the WR dust shell at the given wavelength (correcting for stellar emission when appropriate – see §4.2), and Θ_{FWHM} is the FWHM of the Gaussian fit. Note the 0.68 in the formula is a correction factor which converts a Gaussian FWHM size estimate to the equivalent uniform disk for a better definition of “Surface Brightness.” The final units of S_λ are $\text{W m}^{-2}\mu\text{m}^{-1} \text{ sr}^{-1}$.

Figure 10 shows the observed surface brightness relations. The objects in the survey all appear to follow the same surface brightness relations, indicating all the systems share a similar near-infrared emission mechanism. Assuming the emission comes from optically-thin carbon dust (described by the optical constants of Zubko 1998), we can estimate the color temperature, and we find $T_{\text{color}} \sim 1000 \text{ K}$ (considering the relation between $1.65\mu\text{m}$ and $2.2\mu\text{m}$) and $T_{\text{color}} \sim 650 \text{ K}$ (considering $2.2\mu\text{m}$ and $3.08\mu\text{m}$). The fact that the surface brightness relations can not be described by a single temperature reflects the fact that the dust from a wide range of temperatures contributes to the near-IR emission.

We compared our observed surface brightness relations with the predicted relations from two models. Firstly, we used the radiative transfer code DUSTY (Ivezic et al. 1999) to fit spherically-symmetric dust shell models (assuming uniform outflow and dust constants of Zubko 1998) to the SED. We could vary the amount of dust optical depth and calculate the model surface brightness subject to an overall fit to the SED. We present the calculated surface brightness relations in Figure 10, spanning $\tau_{2.2\mu} = 0.01\text{--}0.77$. We note that the SED fits were not perfect (usually under-predicting $3.1\mu\text{m}$ fluxes), and thus we take these relations as representative but not fully optimized.

Harries et al. (2004) recently calculated the emergent flux from a series of spiral dust shell models using the 3-D (Monte Carlo) radiative transfer code TORUS (Harries 2000). We refer to this as the “WR 104 Reference Model” and used this sophisticated physical model to

calculate the surface brightness relations as a function of inclination angle (the model only reasonably fits the WR 104 SED for low inclinations). These results can also be found on Figure 10.

Comparing the model calculations to the data, we find that neither of these models are a good fit to all the $1.65\mu\text{m}$, $2.2\mu\text{m}$, and $3.1\mu\text{m}$ surface brightness relations, although the models can reproduce some of the observations. More generically, this figure shows us that any particular dust shell geometry yields a family of surface brightness relations. The tightly-correlated surface brightness relations measured for our sample is suggestive of a shared and distinctive dust shell geometry, although neither the spherically-symmetric nor 3-D WR 104 Reference Model can fully explain our results. One could improve the fits of a given model to the data by tuning the adopted optical constants (which are not well known), although the differences *between* models would persist. Before discussing the implications of this, we look for more information in the “size ratio” relations.

5.2. Size Ratio Relations

Another possibly distinctive (and distance-independent) signature to differentiate spherically-symmetric dust shells from colliding wind systems is the ratio of dust shell characteristic sizes at different wavelengths. We have collected all of the size ratios and presented these (with errors) in Figure 11. Assuming all the objects are drawn from the same class, we find the following *mean* size relations:

$$R_{1.65\mu\text{m}/2.2\mu\text{m}} = \frac{\text{FWHM at } 1.65\mu\text{m}}{\text{FWHM at } 2.2\mu\text{m}} = 0.73 \pm 0.05 \quad (7)$$

$$R_{3.08\mu\text{m}/2.2\mu\text{m}} = \frac{\text{FWHM at } 3.08\mu\text{m}}{\text{FWHM at } 2.2\mu\text{m}} = 1.36 \pm 0.07 \quad (8)$$

This compares favorably with calculations for an optically-thin, spherically-symmetric dust shell ($R_{1.65\mu\text{m}/2.2\mu\text{m}} = 0.78$, $R_{3.08\mu\text{m}/2.2\mu\text{m}} = 1.22$), as performed using DUSTY (Ivezic et al. 1999) and tuned to fit the SED. We have also calculated the size ratios predicted by the WR 104 reference model discussed in the last section. As shown in Harries et al. (2004), this model does a remarkable job in fitting the morphology, SED, and overall size. The series of dust shell models used to calculate the size relations (as well as surface brightness relations) can be found in Figure 12. Analysis of these synthetic images yields the following mean size relations:

$$\text{inclination } 0^\circ : \quad R_{1.65\mu\text{m}/2.2\mu\text{m}} = 0.92$$

	$R_{3.08\mu m/2.2\mu m}$	=	1.04
inclination 30° :	$R_{1.65\mu m/2.2\mu m}$	=	0.91
	$R_{3.08\mu m/2.2\mu m}$	=	1.07
inclination 60° :	$R_{1.65\mu m/2.2\mu m}$	=	0.95
	$R_{3.08\mu m/2.2\mu m}$	=	1.14
inclination 90° :	$R_{1.65\mu m/2.2\mu m}$	=	0.98
	$R_{3.08\mu m/2.2\mu m}$	=	1.28

Paradoxically, the simple spherically-symmetric model fits the WR 104 size relations *better* than the model made specifically for WR 104. This can be explained if the optical depth of the shell in the reference model of Harries et al. (2004) is somewhat too high. High τ in the inner windings of the spiral casts a strong shadow across the nebula which cause the temperature profile to be very steep (analogous to the temperature profile for an optically-thick dust shell). Most likely the observed size relations can be accommodated by the pinwheel model by adjusting the distribution of dust in the inner most part of the nebulae.

5.3. Comments on individual objects

WR 112: We know that WR 112 is in a colliding wind binary system (like WR 98a and WR 104) from its clear non-thermal radio emission (Chapman et al. 1999; Monnier et al. 2002b). Furthermore, we believe that we are viewing the binary near the orbital plane (not face-on) because the non-thermal radio emission is highly variable, suggesting that our line-of-sight periodically passes through the optically-thin O-star wind (as is well-documented for WR 140, White & Becker 1995). In this context, it is not surprising that the colliding wind dust spiral takes on a more complicated shape due to projection effects (see discussion of this in Monnier et al. 2002d; Harries et al. 2004). Indeed, the $i = 60^\circ$ model for WR 104 (Figure 12) bears an obvious similarity to the “horseshoe” structure that we observed for WR 112 (middle-panel of Figure 9).

This suggestion of an edge-on viewing angle contradicts the apparent (near) face-on dust spiral geometry seen in the mid-IR (Marchenko et al. 2002). We speculate that projection effects of the outer spiral windings (seen at high inclination) could also explain the mid-IR data, yielding bright arcs and filaments that may resemble a face-on spiral outflow (e.g., Monnier et al. 2002b). Alternatively, if the underlying colliding wind system is indeed viewed from a face-on position as implied by the mid-IR images, then the variable radio emission

might be caused by a, as yet undetected, third stellar component to the system. Further analysis of this system will be included in a future paper where we will present multi-epoch near- and mid-IR images as well as VLA monitoring photometry.

WR 113 CV Ser: van der Hucht (2001) lists WR 113 as a nearly edge-on binary system (inclination $\sim 70^\circ$) with colliding winds. We expect such edge-on systems to show significant dust shell elongations in near-IR (see Figure 12), although our data indicates the dust emission is symmetric (Ratio $r = \text{FWHM}_{\text{minor}}/\text{FWHM}_{\text{major}} \gtrsim 0.8$). This higher level of symmetry could result if the cone opening angle of colliding wind interface was larger than found for WR 104 or if there was significant dust entrained in the WR outflow in a more spherical pattern. Perhaps the hint of a 3rd component in the system (Niemela et al. 1996) could also explain this surprising lack of dust shell asymmetry in this object.

WR 118: Our K-band size estimate is compatible with the earlier speckle measurement of Yudin et al. (2001).

Quintuplet Stars: Tuthill et al. (2006) recently reported resolving two bright Quintuplet WC stars into pinwheel nebulae. These objects show a size ratio $R_{3.08\mu\text{m}/2.2\mu\text{m}} \sim 2$, larger than for the stars reported here, along with a correspondingly low $3.1\mu\text{m}$ surface brightness. We have not included these stars in this paper given the difficulty in correcting for extinction and the possible importance of local heating in this unusually dense and active cluster.

6. Conclusions and Future Work

We have presented a multi-wavelength survey of near-infrared angular sizes of dusty Wolf-Rayet systems from the Keck Aperture Masking program. Aperture synthesis images were presented for WR 112 for the first time and we found strong evidence for interacting/colliding winds. In addition, we presented new epochs of WR 104 and WR 98a images as well as the first results at $3.1\mu\text{m}$, confirming the spiral nature of the dust shells for WR 104 and WR 98.

Using these data, we discovered tightly-correlated surface brightness relations and also common size ratios between different near-infrared bands. The observed relations could not be reproduced in detail using either a spherically-symmetric dust shell model or the 3-D radiative transfer model of WR 104 (Harries et al. 2004). The high-quality data presented here will act as an observational foundation for a new generation of modelling efforts.

We find these results to be compelling *indirect* evidence that all these dusty WR here

share a common emission geometry, presumably related to the obvious spiral distribution of WR 104 and WR 98a (and confirmed recently for two Quintuplet WC stars; Tuthill et al. 2006). Thus, while not conclusive, this study can be viewed as further evidence that WC Wolf-Rayet stars are associated with binarity (Monnier et al. 1999a; Williams & van der Hucht 2000).

In order to make further progress on identifying binarity, we must pursue multiple approaches. While traditional direct spectroscopic identifications of binarity have proved difficult (e.g., Williams & van der Hucht 2000), other promising methods have emerged for unambiguously determining if dusty WR systems are binaries. We recommend the following strategies be pursued:

- Higher resolution infrared data. A factor of 3 longer baselines will allow unambiguous detection of asymmetry and non-zero closure phases, if spirals and/or filaments exist in our sample. This corresponds to about 30 m baselines, easily achievable with the current interferometers (the Very Large Telescope is particularly well-suited to this). The main challenge will be the low visible flux which makes tip-tilt tracking difficult – infrared star trackers would be helpful in this regard.
- Visible or infrared photometry. Photometric fluctuations have been reported for WR 98a (Monnier et al. 1999a) and WR 104 (Kato et al. 2002). The variations seem to correlate to the known orbital periods and we strongly encourage observers to monitor all dusty WC stars to establish the periods of the putative underlying binaries. This method can work for objects at large distances (e.g., galactic center, Local Group), however one has to contend with intrinsic variability and have the determination to monitor sources over many years (or decades; Williams et al. 1990a).
- Non-thermal radio emission. For systems with periods $\gtrsim 1$ year, we expect detectable non-thermal radio emission from the colliding winds (Dougherty & Williams 2000b; Monnier et al. 2002c). This requires sensitive measurements at multiple frequencies but should be possible and will yield unambiguous results. Recent successful attempts to use this method include Leitherer et al. (1997), Chapman et al. (1999), Monnier et al. (2002b), and Cappa et al. (2004).

While skeptics will not be convinced yet that the WC phenomena has a necessary connection to binarity, the evidence in favor of this scenario continues to accumulate. The proposed observational efforts to conclusively establish binarity complement on-going theoretical studies to explore the far-reaching consequences of the role of binarity in the theory of massive star evolution. Indeed, a complete understanding of Gamma Ray Burst progenitors,

the Galactic Black Hole population, and the high-mass end of the Initial Mass Function hinges on an accurate picture of massive binary stellar evolution.

This work would not have been possible without the support of Dr. Charles Townes (U.C. Berkeley); much of data in this paper were acquired during observing time granted to him. This research has made use of the SIMBAD database, operated at CDS, Strasbourg, France. This publication makes use of data products from the Two Micron All Sky Survey (2MASS), which is a joint project of the University of Massachusetts and the Infrared Processing and Analysis Center/California Institute of Technology, funded by the National Aeronautics and Space Administration and the National Science Foundation. The data presented herein were obtained at the W.M. Keck Observatory, which is operated as a scientific partnership among the California Institute of Technology, the University of California and the National Aeronautics and Space Administration. The Keck Observatory was made possible by the generous financial support of the W.M. Keck Foundation. The authors wish to recognize and acknowledge the very significant cultural role and reverence that the summit of Mauna Kea has always had within the indigenous Hawaiian community. We are most fortunate to have the opportunity to conduct observations from this mountain.

REFERENCES

- Cappa, C., Goss, W. M., & van der Hucht, K. A. 2004, *AJ*, 127, 2885
- Chapman, J. M., Leitherer, C., Koribalski, B. ., Bouter, R., & Storey, M. 1999, *ApJ*, 518, 890
- Cherchneff, I., Le Teuff, Y. H., Williams, P. M., & Tielens, A. G. G. M. 2000, *A&A*, 357, 572
- Cutri, R. M., Skrutskie, M. F., van Dyk, S., Beichman, C. A., Carpenter, J. M., Chester, T., Cambresy, L., Evans, T., Fowler, J., Gizis, J., Howard, E., Huchra, J., Jarrett, T., Kopan, E. L., Kirkpatrick, J. D., Light, R. M., Marsh, K. A., McCallon, H., Schneider, S., Stiening, R., Sykes, M., Weinberg, M., Wheaton, W. A., Wheelock, S., & Zacarias, N. 2003, *VizieR Online Data Catalog*, 2246, 0
- Danchi, W. C., Tuthill, P. G., & Monnier, J. D. 2001, *ApJ*, 562, 440
- de Marco, O. & Schmutz, W. 1999, *A&A*, 345, 163
- De Marco, O., Schmutz, W., Crowther, P. A., Hillier, D. J., Dessart, L., de Koter, A., & Schweickhardt, J. 2000, *A&A*, 358, 187

- Dougherty, S. M., Beasley, A. J., Claussen, M. J., Zauderer, B. A., & Bolingbroke, N. J. 2005, *ApJ*, 623, 447
- Dougherty, S. M. & Williams, P. M. 2000a, *MNRAS*, 319, 1005
- . 2000b, *MNRAS*, 319, 1005
- Efron, B. & Tibshirani, R. J. 1993, *An introduction to the bootstrap* (New York: Chapman and Hall)
- ESA. 1997, *VizieR Online Data Catalog*, 1239, 0
- Gull, S. F. & Skilling, J. 1983, in *Indirect Imaging. Measurement and Processing for Indirect Imaging. Proceedings of an International Symposium held in Sydney, Australia, August 30-September 2, 1983*. Editor, J.A. Roberts; Publisher, Cambridge University Press, Cambridge, England, New York, NY, 1984. LC # QB51.3.E43 I53 1984. ISBN # 0-521-26282-8. P.267, 1983, 267+
- Harries, T. J. 2000, *MNRAS*, 315, 722
- Harries, T. J., Monnier, J. D., Symington, N. H., & Kurosawa, R. 2004, *MNRAS*, 350, 565
- Harrison, W. & Goodrich, R. W. 1999, *The NIRC User’s Manual*, maintained by the Keck Observatory
- Ivezic, Z., Nenkova, M., & Elitzur, M. 1999, *User Manual for DUSTY*, Tech. rep., University of Kentucky
- Kato, T., Haseda, K., Yamaoka, H., & Takamizawa, K. 2002, *PASJ*, 54, L51
- Leitherer, C., Chapman, J. M., & Koribalski, B. 1997, *ApJ*, 481, 898
- Marchenko, S. V., Moffat, A. F. J., Vacca, W. D., Côté, S., & Doyon, R. 2002, *ApJ*, 565, L59
- Matthews, K., Ghez, A. M., Weinberger, A. J., & Neugebauer, G. 1996, *PASP*, 108, 615+
- Millan-Gabet, R., Schloerb, F. P., & Traub, W. A. 2001, *ApJ*, 546, 358
- Moffat, A. F. J., Lamontagne, R., Williams, P. M., Horn, J., & Seggewiss, W. 1987, *ApJ*, 312, 807
- Monnier, J. D., Greenhill, L. J., Tuthill, P. G., & Danchi, W. C. 2002a, in *ASP Conf. Ser. 260: Interacting Winds from Massive Stars*, ed. A. F. J. Moffat & N. St-Louis, 331–+

- Monnier, J. D., Greenhill, L. J., Tuthill, P. G., & Danchi, W. C. 2002b, *ApJ*, 566, 399
- . 2002c, *ApJ*, 566, 399
- Monnier, J. D., Millan-Gabet, R., Billmeier, R., Akeson, R. L., Wallace, D., Berger, J.-P., Calvet, N., D’Alessio, P., Danchi, W. C., Hartmann, L., Hillenbrand, L. A., Kuchner, M., Rajagopal, J., Traub, W. A., Tuthill, P. G., Boden, A., Booth, A., Colavita, M., Gathright, J., Hrynevych, M., Le Mignant, D., Ligon, R., Neyman, C., Swain, M., Thompson, R., Vasisht, G., Wizinowich, P., Beichman, C., Beletic, J., Creech-Eakman, M., Koresko, C., Sargent, A., Shao, M., & van Belle, G. 2005, *ApJ*, 624, 832
- Monnier, J. D., Millan-Gabet, R., Tuthill, P. G., Traub, W. A., Carleton, N. P., Coudé du Foresto, V., Danchi, W. C., Lacasse, M. G., Morel, S., Perrin, G., Porro, I. L., Schloerb, F. P., & Townes, C. H. 2004, *ApJ*, 605, 436
- Monnier, J. D., Tuthill, P. G., & Danchi, W. C. 1999a, *ApJ*, 525, L97
- . 1999b, *ApJ*, 525, L97
- . 2002d, *ApJ*, 567, L137
- Monnier, J. D., Tuthill, P. G., Lopez, B., Cruzalebes, P., Danchi, W. C., & Haniff, C. A. 1999c, *ApJ*, 512, 351
- Niemela, V. S., Morrell, N. I., Barba, R. H., & Bosch, G. L. 1996, in *Revista Mexicana de Astronomia y Astrofisica Conference Series*, ed. V. Niemala & N. Morrell, 100–+
- Pauls, T. A., Young, J. S., Cotton, W. D., & Monnier, J. D. 2005, *PASP*, 117, 1255
- Ragland, S. & Richichi, A. 1999, *MNRAS*, 302, L13
- Rajagopal, J. K., Barry, R., Lopez, B., Danchi, W. C., Monnier, J. D., Tuthill, P. G., & Townes, C. H. 2004, in *New Frontiers in Stellar Interferometry*, *Proceedings of SPIE Volume 5491*. Edited by Wesley A. Traub. Bellingham, WA: The International Society for Optical Engineering, 2004., p.1120, ed. W. A. Traub, 1120–+
- Sivia, D. 1987, PhD thesis, Cambridge University
- Skilling, J. & Bryan, R. K. 1984, *MNRAS*, 211, 111+
- Tuthill, P., Monnier, J., Tanner, A., Figier, D., & Ghez, A. 2006, *Science*, in press
- Tuthill, P. G., Monnier, J. D., & Danchi, W. C. 1999a, *Nature*, 398, 487

- . 1999b, *Nature*, 398, 487
- Tuthill, P. G., Monnier, J. D., Danchi, W. C., & Lopez, B. 2000a, *ApJ*, in press
- Tuthill, P. G., Monnier, J. D., Danchi, W. C., Wishnow, E., & Haniff, C. A. 2000b, *PASP*, in press
- Tuthill, P. G., Monnier, J. D., Danchi, W. C., Wishnow, E. H., & Haniff, C. A. 2000c, *PASP*, 112, 555
- Usov, V. V. 1991, *MNRAS*, 252, 49
- van der Hucht, K. A. 2001, *New Astronomy Review*, 45, 135
- White, R. L. & Becker, R. H. 1995, *ApJ*, 451, 352
- Williams, P. M. & van der Hucht, K. A. 2000, *MNRAS*, 314, 23
- Williams, P. M., van der Hucht, K. A., Pollock, A. M. T., Florkowski, D. R., van der Woerd, H., & Wamsteker, W. M. 1990a, *MNRAS*, 243, 662
- Williams, P. M., van der Hucht, K. A., Pollock, A. M. T., Florkowski, D. R., van der Woerd, H., & Wamsteker, W. M. 1990b, *MNRAS*, 243, 662
- Williams, P. M., van der Hucht, K. A., & The, P. S. 1987, *A&A*, 182, 91
- Yudin, B., Balega, Y., Blöcker, T., Hofmann, K.-H., Schertl, D., & Weigelt, G. 2001, *A&A*, 379, 229
- Zubko, V. G. 1998, *MNRAS*, 295, 109+

Table 1. Properties of NIRC Camera Infrared Filters

Name	Center Wavelength λ_0 (μm)	Bandpass FWHM $\Delta\lambda$ (μm)	Fractional Bandwidth
FeII	1.6471	0.0176	1.1%
H	1.6575	0.333	20%
K	2.2135	0.427	19%
Kcont	2.25965	0.0531	2.3%
CH4	2.269	0.155	6.8%
PAHcs	3.0825	0.1007	3.3%

Note. — Reference: The NIRC Manual (Harrison & Goodrich 1999)

Table 2. Basic Properties of Targets

Source Names	RA (J2000)	Dec (J2000)	V mag ^a	J mag ^a	H mag ^a	K mag ^a	Spectral Type	Distance (kpc)	Luminosity Log (L/L _⊙) ^b	Photometry References
γ ² Vel, WR 11	08 09 31.96	-47 20 11.8	1.81	2.15	2.25	2.10	WC8 + O7.5III-V (1)	0.26 (2)	5.5 ^c (3,4)	5
WR 48a	13 12 39.65	-62 42 55.8		8.74	6.80	5.09	WC8ed + ? (1)	1.2 (1)		5,9
WR 76	16 40 05.3	-45 41 10	15.36	8.46	6.51	4.88	WC9d (1)	5.35 (1)		5,9
WR 95	17 36 19.76	-33 26 10.9	14.00	8.29	6.67	5.27	WC9d (1)	2.09 (1)		5,9
WR 98a	17 41 13.051	-30 32 30.34		9.14	6.51	4.33	WC8-9vd + OB? (1)	1.9 (8)		9
WR 104	18 02 04.123	-23 37 42.24	13.54	6.67	4.34	2.42	WC9d + B0.5V (1)	2.3 (6)	5.4 ^c (7)	5
WR 106	18 04 43.66	-21 09 30.7	11.93	7.94	6.28	4.82	WC9d (1)	2.3 (1)		5,9
WR 112	18 16 33.489	-18 58 42.47	17.7	8.68	6.26	4.26	WC9d + OB? (1)	4.15 (1)		5,9
WR 113	18 19 07.36	-11 37 59.2	9.43	7.02	6.28	5.49	WC8d + O8-9 (1)	1.79 (1)		5,9
WR 118	18 31 42.3	-09 59 15	22	8.10	5.41	3.65	WC9 (1)	3.13 (1)		5,9,10
WR 140	20 20 27.98	+43 51 16.3	6.9	5.55	5.43	5.04	WC7pd + O4-5 (1)	1.85 (11)	6.1 ^c (12)	–

^a These magnitudes (V band from Simbad, and J,H,K bands from 2MASS) are merely representative since some of the targets are variable.

^b Luminosity here has been corrected for the adopted distance used in this paper; not all objects have well-established luminosities due to high extinction.

^c Binary system total luminosity.

Note. — References: (1) van der Hucht (2001), (2) ESA (1997), (3) De Marco et al. (2000), (4) de Marco & Schmutz (1999), (5) Williams et al. (1987), (6) Tuthill et al. (1999a), (7) Harries et al. (2004), (8) Monnier et al. (1999b), (9) 2MASS; Cutri et al. (2003), (10) Simbad, (11) Dougherty et al. (2005), (12) Williams et al. (1990a)

Table 3. Journal of Observations

Target	Date (UT)	Filter (λ_o) (μm)	Aperture Mask	Calibrator ^a Names
γ^2 Vel	1999 Feb 05	CH4 (2.269)	Golay-21	HD 68553 (K3, 4.39 ± 0.44 mas)
WR 48a	2000 Jan 26	K (2.2135)	Annulus-36	HD 115399 (K5, 1.2 ± 0.7 mas)
WR 76	1998 Jun 05	H (1.6575)	Annulus-36	HD 151834 (G3, 1.2 ± 0.4 mas)
		K (2.2135)		
		CH4 (2.269)		
WR 95	1999 Apr 26	H (1.6575)	Annulus-36	HD 153258 (K4, 2.4 ± 0.9 mas)
		K (2.2135)		
		PAHcs (3.0825)		
		H (1.6575)		
WR 98a	2000 Jun 24	K (2.2135)	Annulus-36	HD 158774
		H (1.6575)		
WR 104	2000 Jun 24	K (2.2135)	Annulus-36	HD 163428 (K5, 4.1 ± 1.0 mas)
		CH4 (2.269)		
		PAHcs (3.0825)		
		H (1.6575)		
WR 106	1998 Jun 05	CH4 (2.269)	Annulus-36	HD 165813 (M0, 1.7 ± 0.9 mas)
		PAHcs (3.0825)		
		H (1.6575)		
		CH4 (2.269)		
WR 112	1999 Jul 30	PAHcs (3.0825)	Annulus-36	HD 167036 (K2, 3.0 ± 0.6 mas)
		K (2.2135)		
		PAHcs (3.0825)		
		H (1.6575)		
WR 113	2000 Jun 24	CH4 (2.269)	Annulus-36	HD 167036
		PAHcs (3.0825)		
		H (1.6575)		
WR 118	1998 Jun 05	K (2.2135)	Annulus-36	HD 168366 (K2, 1.03 ± 0.12 mas)
		CH4 (2.269)		
		PAHcs (3.0825)		
		H (1.6575)		
WR 140	1999 Jul 30	CH4 (2.269)	Annulus-36	HD 175775 (K0, 3.5 ± 1.1 mas)
		PAHcs (3.0825)		
		H (1.6575)		
		CH4 (2.269)		
WR 140	2001 Jul 30	PAHcs (3.0825)	Annulus-36	HD 170474 (K0, 1.3 ± 0.3 mas)
		FeII (1.6471)		
		Kcont (2.25965)		
		FeII (1.6471)		
WR 140	2001 Jul 30	CH4 (2.269)	Annulus-36	HD 173074 (M, 3.4 ± 1.4 mas)
		PAHcs (3.0825)		
		H (1.6575)		
		CH4 (2.269)		
WR 140	2001 Jul 30	PAHcs (3.0825)	Annulus-36	HD 175775
		FeII (1.6471)		
		Kcont (2.25965)		
		FeII (1.6471)		
WR 140	2001 Jul 30	CH4 (2.269)	Annulus-36	HD 168000
		PAHcs (3.0825)		
		H (1.6575)		
		CH4 (2.269)		
WR 140	2001 Jul 30	PAHcs (3.0825)	Annulus-36	HD 175775
		FeII (1.6471)		
		Kcont (2.25965)		
		FeII (1.6471)		
WR 140	2001 Jul 30	CH4 (2.269)	Annulus-36	HD 192867 (M1, 1.6 ± 0.6 mas)
		PAHcs (3.0825)		
		H (1.6575)		
		CH4 (2.269)		
WR 140	2001 Jul 30	PAHcs (3.0825)	Annulus-36	HD 192867
		FeII (1.6471)		
		Kcont (2.25965)		
		FeII (1.6471)		

^aCalibrator size estimates made using *getCal*, maintained and distributed by the Michelson Science Center (<http://msc.caltech.edu>).

Table 4. Mean Infrared Size Results

Target	Date (UT)	Gaussian FWHM (mas) ^{a,b}			Comments
		1.65 μ m	2.2 μ m	3.08 μ m	
γ^2 Vel	1999 Feb 05	–	7 \pm 7	–	
WR 48a	2000 Jan 26	–	63 \pm 3 ^(c)	–	Fit to “large-scale” component only.
WR 76	1998 Jun 05	17 \pm 3	19 \pm 4	–	
	1999 Apr 26	19 \pm 3	20 \pm 4	21 \pm 4	
WR 95	2000 Jun 24	16 \pm 3 ^(c)	23 \pm 4 ^(c)	–	
WR 98a	2000 Jun 24	73 \pm 4 ^(c)	110 \pm 7	147 \pm 9	Fit to “large-scale” component only.
		r=0.56	r=0.74	r=0.81	Elliptical (PA \sim 120 $^\circ$).
WR 104	2000 Jun 24	57 \pm 9	73 \pm 7	101 \pm 9	Fit to “large-scale” component only.
		r=0.84	r=0.88	r=0.85	Elliptical (PA \sim 30 $^\circ$).
WR 106	1998 Jun 05	17 \pm 3 ^(c)	23 \pm 4 ^(c)	33 \pm 3	
	1999 Jul 30	–	21 \pm 4 ^(c)	24 \pm 4	
WR 112	2000 Jun 24	40 \pm 10	83 \pm 7	131 \pm 9	Fit to “large-scale” component only.
			r=0.87		Elliptical (PA \sim 130).
WR 113	2000 Jun 24	19 \pm 2 ^(c)	27 \pm 3 ^(c)	–	
WR 118	1998 Jun 05	18 \pm 3	24 \pm 4	30 \pm 3	
	1998 Jun 06	18 \pm 3	23 \pm 4	32 \pm 3	
	1999 Apr 26	21 \pm 3	23 \pm 4	33 \pm 3	
WR 140	1999 Jul 30	<15	<13	–	Pre-outburst
	2001 Jul 30	268 \pm 17 39% dust	228 \pm 12 64% dust	263 \pm 13 78% dust	Two-component model: Gaussian + Point

^aThese characteristic sizes are *not* corrected for the presence of the star (which contribute significant near-IR flux in some cases).

^bIf visibility data are manifestly elliptical, then we report both the mean FWHM and the Ratio $r = \text{FWHM}_{\text{minor}}/\text{FWHM}_{\text{major}}$.

^cSee Table 5 for corrected sizes.

Table 5. Characteristic sizes of Wolf-Rayet dust shells, corrected for stellar contribution

Target	Dust Fraction (%)		Gaussian FWHM (mas) ^a	
	1.65 μ m	2.2 μ m	1.65 μ m	2.2 μ m
WR 48a	–	85%	–	70 \pm 5
WR 95	73%	89%	19 \pm 4	25 \pm 4
WR 98a	90%	–	78 \pm 5	–
WR 106	78%	93%	20 \pm 4	24 \pm 5
	–	93%	–	22 \pm 5
WR 113	38%	65%	35 \pm 10	35 \pm 6

^aThese characteristic sizes are corrected for the presence of the star (which contribute significant near-IR flux in some cases; see §4.2). Refer to Table 4 for size measurements for rest of sample which do not require corrections.

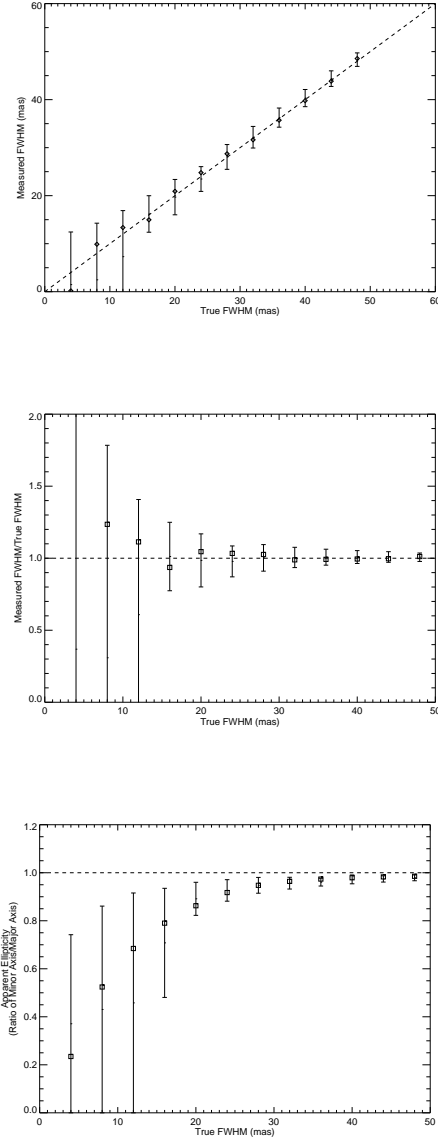


Fig. 1.— These graphs show the results for the fitting of simulated data using calibrators from the June 2000 epoch for the CH4 band using the Annulus mask. The top panel shows the measured Gaussian FWHM from the simulated data compared to the input model. The middle panel re-displays this information as a ratio. The bottom panel explores how miscalibration induces ellipticity into the fits, even for an input circular Gaussian. The dashed lines indicate the position of the original simulated data. All error bars indicate $1\text{-}\sigma$ certainty and data points indicate medians.

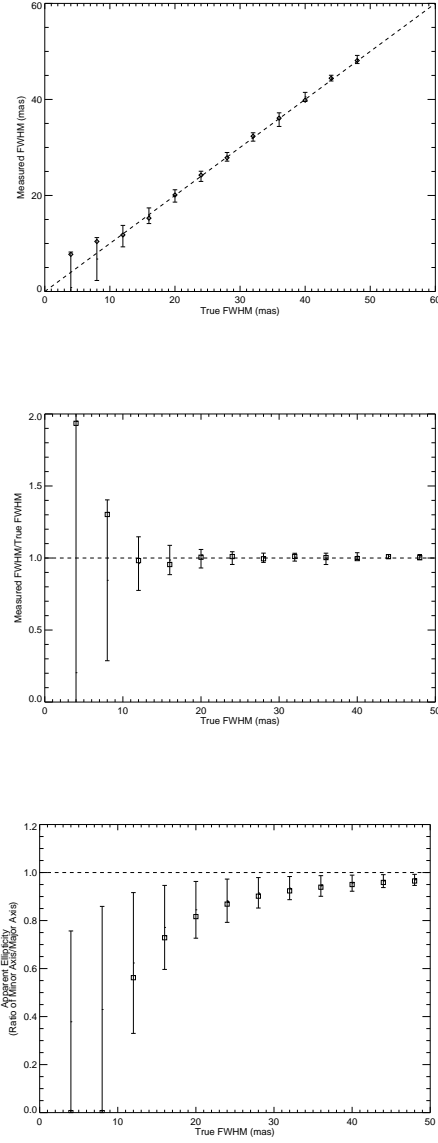


Fig. 2.— These graphs show the results for the fitting of recalibrated simulated data using calibrators from the June 2000 epoch for the H band using the Annulus mask. The format of the plots are the same as previous figure.

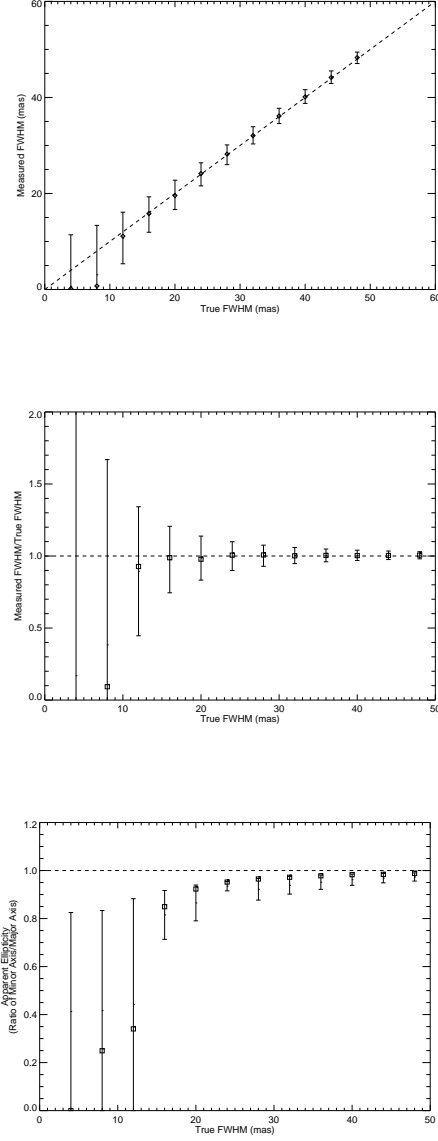


Fig. 3.— These graphs show the results for the fitting of recalibrated simulated data using calibrators from the June 2000 epoch for the PAHcs band using the Annulus mask. The format of the plots are the same as previous figure.

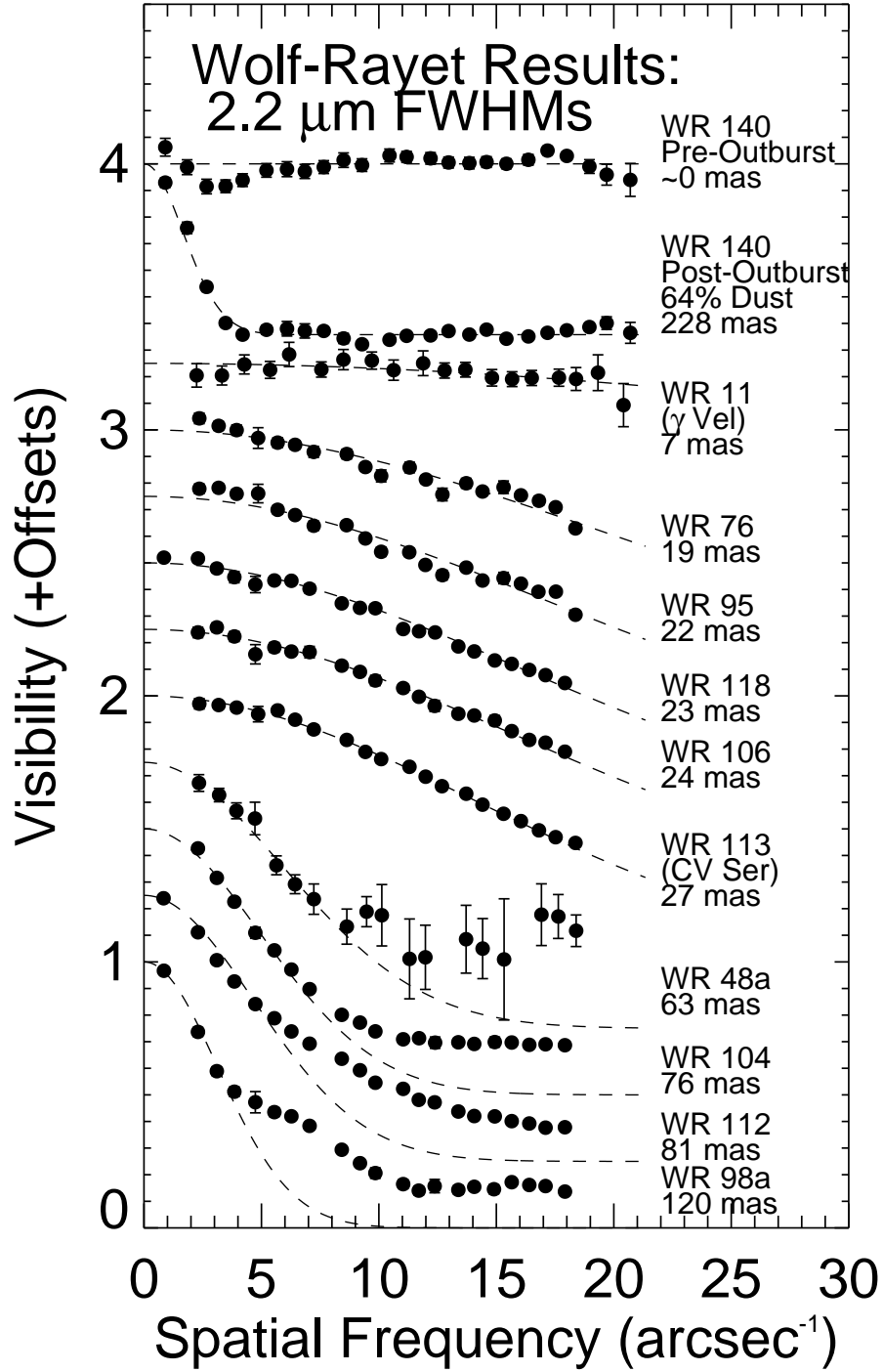


Fig. 4.— This figure shows the azimuthally-averaged visibility curves at $2.2\mu\text{m}$ for Wolf-Rayet stars in our sample, along with best-fit Gaussian curves. Each visibility curve is offset by 0.25 from the next. For the most resolved dust shells, the Gaussian curves were only fitted to the “large-scale” component of the visibility data ($V > 0.5$). See Table 4 for detailed fitting results.

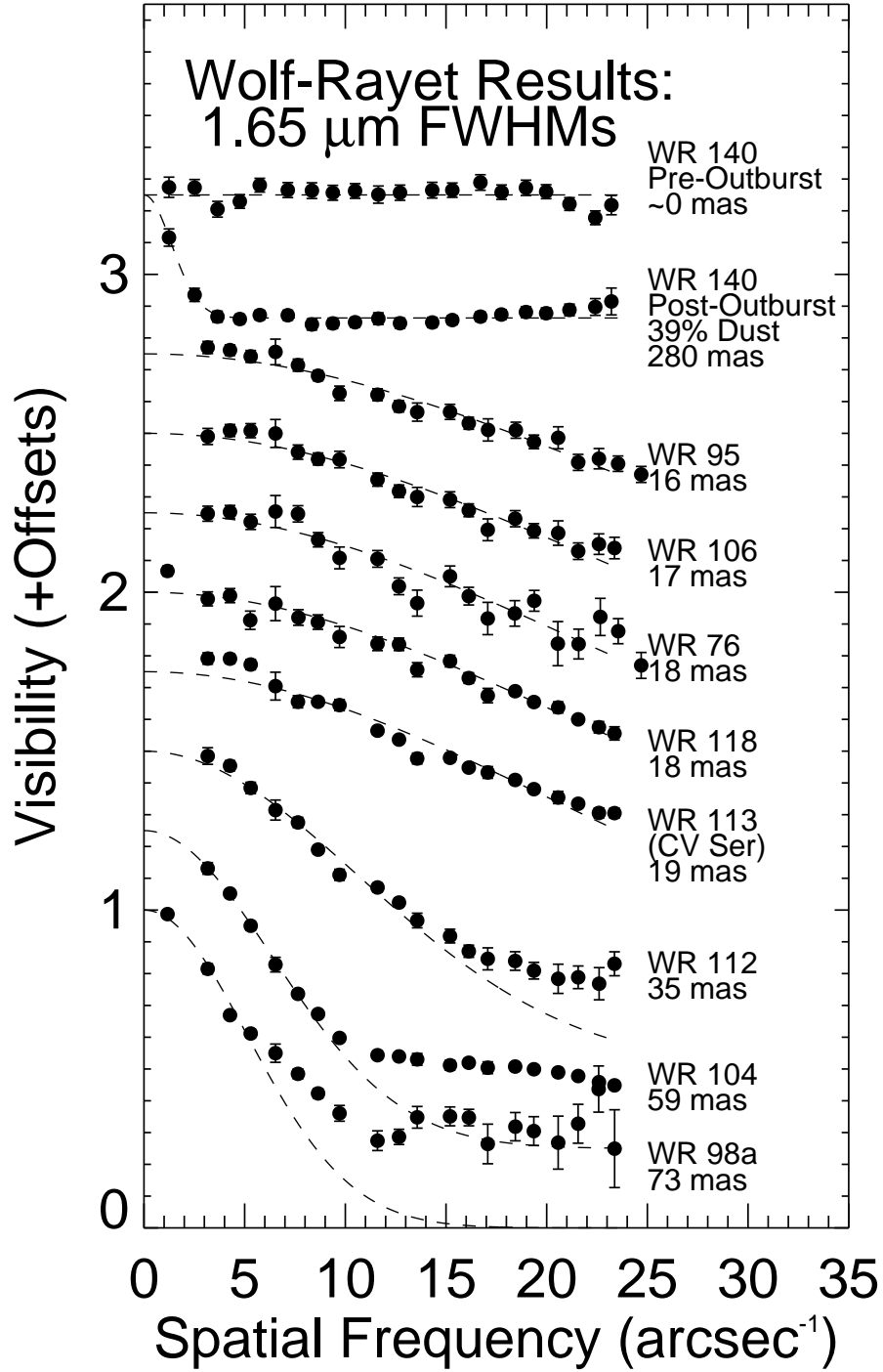


Fig. 5.— This figure shows the azimuthally-averaged visibility curves at $1.65\mu\text{m}$ for Wolf-Rayet stars in our sample, along with best-fit Gaussian curves. Each visibility curve is offset by 0.25 from the next. For the most resolved dust shells, the Gaussian curves were only fitted to the “large-scale” component of the visibility data ($V > 0.5$). See Table 4 for detailed fitting results.

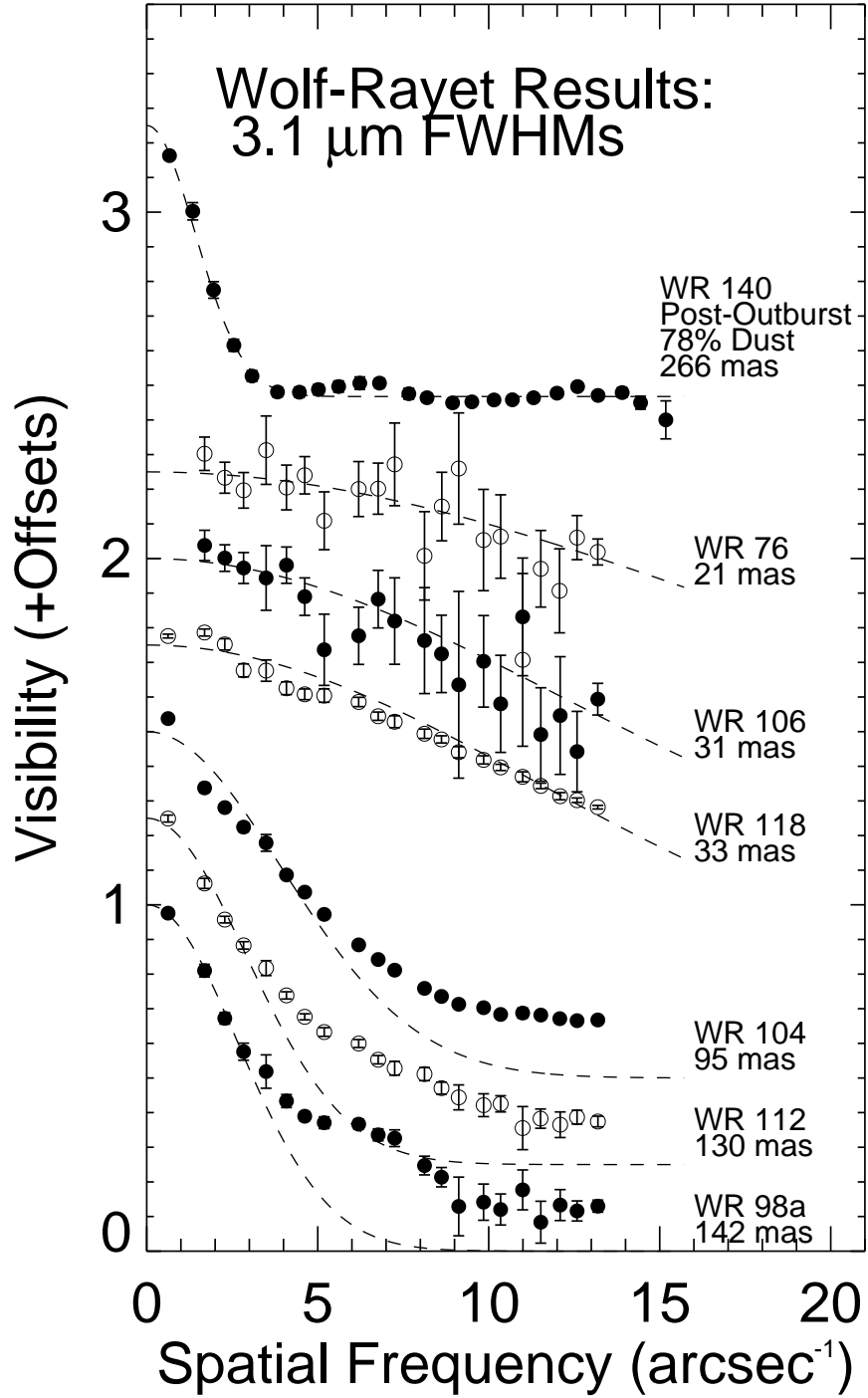


Fig. 6.— This figure shows the azimuthally-averaged visibility curves at $3.1\mu\text{m}$ for Wolf-Rayet stars in our sample, along with best-fit Gaussian curves. Each visibility curve is offset by 0.25 from the next. For the most resolved dust shells, the Gaussian curves were only fitted to the “large-scale” component of the visibility data ($V > 0.5$). See Table 4 for detailed fitting results.

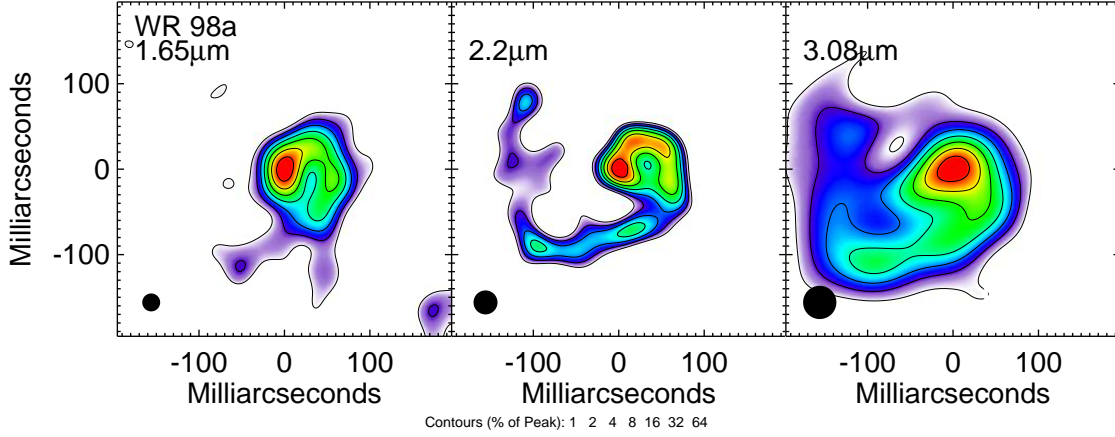


Fig. 7.— Here we show multiwavelength aperture synthesis images of WR 98a on UT 2000 Jun 24, at $1.65\mu\text{m}$, $2.2\mu\text{m}$, and $3.08\mu\text{m}$. Note that the resolution is lower at the longer wavelengths, as indicated by the “beam” spot located in the bottom-left corner of each panel (representing the best achievable angular resolution, $\Delta\Theta = \frac{\lambda}{2B_{\text{max}}}$).

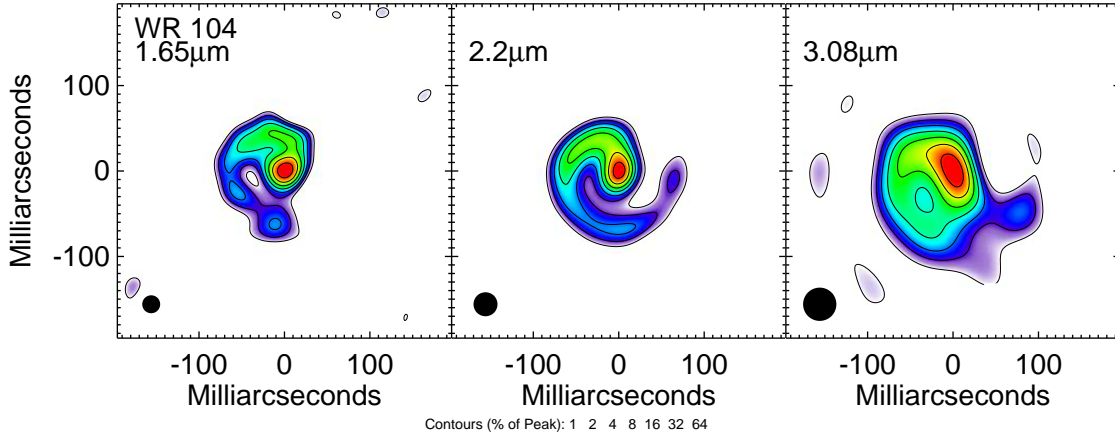


Fig. 8.— Here we show multiwavelength aperture synthesis images of WR 104 on UT 2000 Jun 24, at $1.65\mu\text{m}$, $2.2\mu\text{m}$, and $3.08\mu\text{m}$. Note that the resolution is lower at the longer wavelengths, as indicated by the “beam” spot located in the bottom-left corner of each panel (representing the best achievable angular resolution, $\Delta\Theta = \frac{\lambda}{2B_{\text{max}}}$).

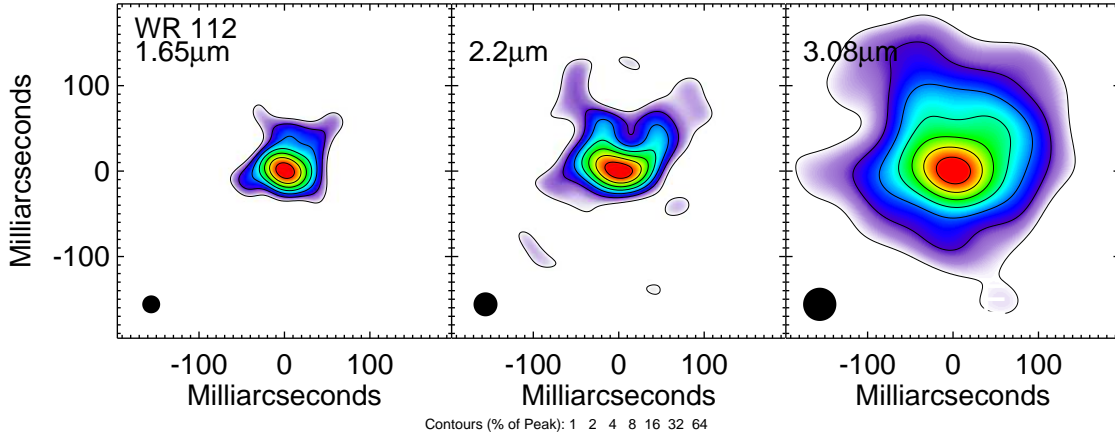


Fig. 9.— Here we show multiwavelength aperture synthesis images of WR 112 on UT 2000 Jun 24, at $1.65\mu\text{m}$, $2.2\mu\text{m}$, and $3.08\mu\text{m}$. Note that the resolution is lower at the longer wavelengths, as indicated by the “beam” spot located in the bottom-left corner of each panel (representing the best achievable angular resolution, $\Delta\Theta = \frac{\lambda}{2B_{\text{max}}}$).

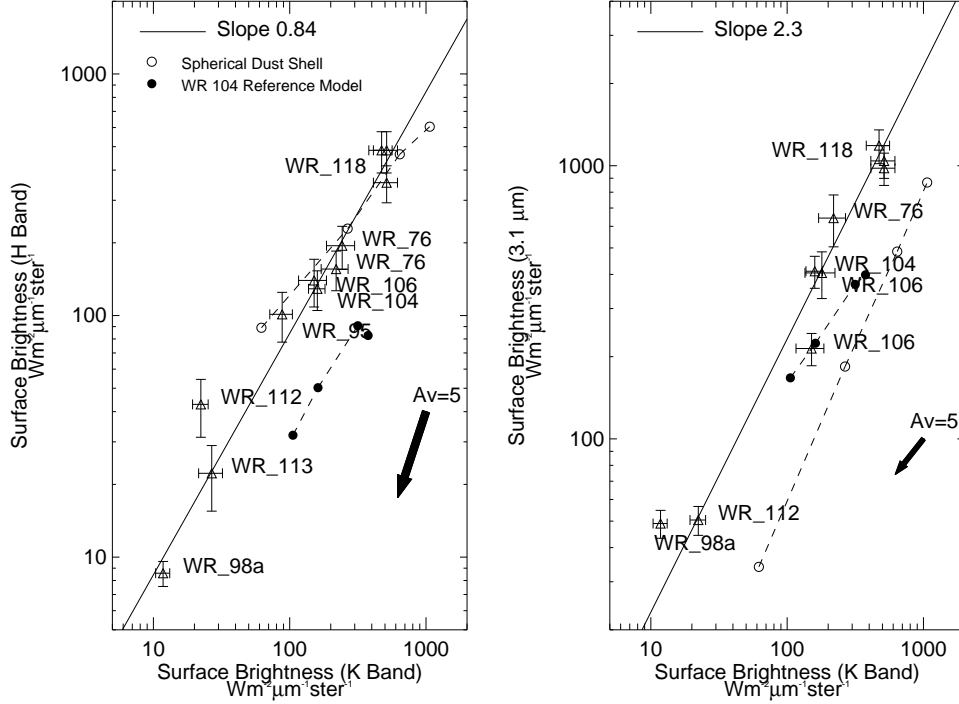


Fig. 10.— Here we show the surface brightness relations for dusty Wolf-Rayet systems. We plot the best-fit linear relation corresponding to $T_{\text{color}} \sim 1000\text{ K}$ (left panel) and $T_{\text{color}} \sim 650\text{ K}$ (right panel), assuming optical constants for Zubko (1998) dust. The open circles show the surface brightness relations for a series of spherically-symmetric dust shell models with $\tau_{2.2\mu} = 0.01, 0.1, 0.3, 0.67$ (higher τ yields higher S_λ). The filled circles show the same relations for the WR 104 Reference Model of Harries et al. (2004) for inclination angles of $i = 0, 30, 60, 90^\circ$ (higher i yields higher S_λ). The arrow shows how the surface brightness changes for interstellar reddening of $A_V = 5$, assuming standard ISM dust.

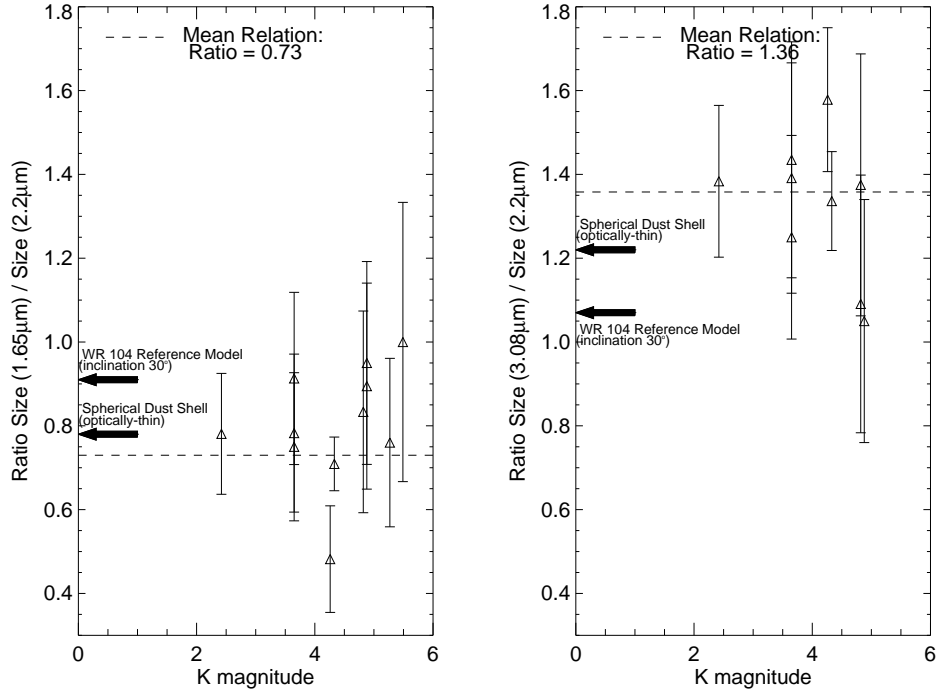


Fig. 11.— Here we plot near-infrared characteristic size ratios vs K-band magnitude. The left panel shows the results for $\frac{\text{FWHM at } 1.65\mu\text{m}}{\text{FWHM at } 2.2\mu\text{m}}$, while the right panel shows the results for $\frac{\text{FWHM at } 3.08\mu\text{m}}{\text{FWHM at } 2.2\mu\text{m}}$. We plot (dashed line) the mean size ratio and also mark with arrows the expected size ratios for (a) optically-thin, spherically-symmetric dust shell and (b) the WR 104 “Reference Model” of Harries et al. (2004) viewed from 30° inclination angle.

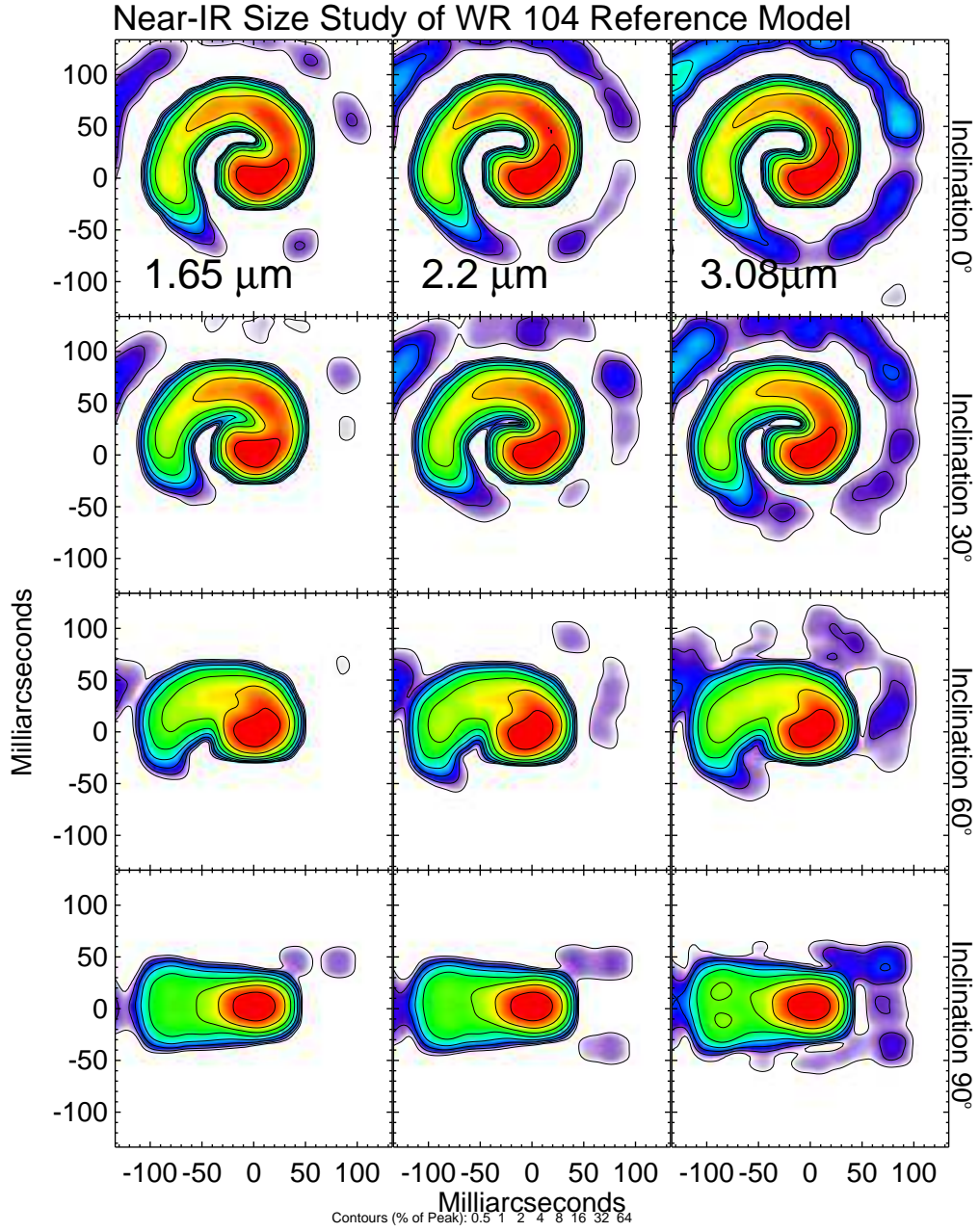


Fig. 12.— Near-IR Size Study of WR 104 Reference Model. This figure shows a gallery of synthetic images of the WR 104 reference model described in Harries et al. (2004), smoothed to a uniform angular resolution of 20 mas. These images were used to derive the surface brightness and size ratio comparisons described in §5.1 & 5.2. The 3 columns correspond to effective wavelengths of $1.65\mu\text{m}$, $2.2\mu\text{m}$, and $3.08\mu\text{m}$, while the 4 rows correspond to viewing angles of inclination 0° , 30° , 60° , and 90° .